

LAVA Simulations for the 3rd AIAA CFD High Lift Prediction Workshop with Body Fitted Grids

James C. Jensen*

NASA Ames Research Center, Moffet Field, CA, 94035

Gerrit-Daniel Stich*

Science and Technology Corporation, Moffet Field, CA, 94035

Jeffrey A. Housman*, Marie Denison*, and Cetin C. Kiris[†]

NASA Ames Research Center Moffett Field, CA 94035

In response to the 3rd AIAA CFD High Lift Prediction Workshop, the workshop cases were analyzed using Reynolds-averaged Navier-Stokes flow solvers within the Launch Ascent and Vehicle Aerodynamics (LAVA) solver framework. For the workshop cases the advantages and limitations of both overset-structured and unstructured polyhedral meshes were assessed. The workshop included 3 cases: a 2D airfoil validation case, a mesh convergence study using the High Lift Common Research Model, and a nacelle/pylon integration study using the JAXA Standard Model. The 2D airfoil case from the workshop is used to verify the implementation of the Spalart-Allmaras turbulence model along with some of its variants within the solver. The High Lift Common Research Model case is used to assess solver performance and accuracy at varying mesh resolutions, as well as identify the minimum mesh fidelity required for LAVA on this class of problem. The JAXA Standard Model case is used to assess the solver's sensitivity to the turbulence model and to compare the structured and unstructured mesh paradigms. These workshop cases have helped establish best practices for high lift flow configurations for the LAVA solver.

I. Nomenclature

α	=	aircraft angle of attack
C_D	=	drag coefficient
C_L	=	lift coefficient
C_M	=	pitching-moment coefficient
C_p	=	pressure coefficient
MAC	=	mean aerodynamic chord
MRC	=	moment reference center

II. Introduction

The use of Computational Fluid Dynamics (CFD) in the design and analysis process for modern transport aircraft has ensured that it is a critical area of interest to those who are looking to use CFD to mitigate costs associated with development of these types of aircraft. The cost mitigation of CFD can be mostly attributed

*Research Scientist, Computational Aerosciences Branch, NAS Division, AIAA Member

[†]Branch Chief, Computational Aerosciences Branch, NAS Division, AIAA Senior Member

to its ability to be used to reduce the number of wind tunnel experiments and expensive tests during the development and certification process. Thus, ensuring the accuracy and validity of CFD tools across the entire flight envelope is essential to justifying its use as a replacement to real world data collection methods. As shown in the AIAA 6th Drag Prediction Workshop,¹ using the current best practices with CFD tools can yield accurate predictions within the cruise region of the flight envelope. The takeoff and landing portion of the flight envelope remains a challenging problem for the CFD community due to the complexity of the physics within the flow field and the complexities of the high-lift device geometries themselves. In order to address these challenges, the AIAA High Lift Prediction Workshops^{2,3,4} created a set of common test cases that the community can use to evaluate their state-of-the-art methods. This workshop allows mutually beneficial collaboration within the community, with the ultimate goal of improving CFD technology so that it can be used more widely throughout the aircraft development process.

The main objectives of the 3rd High Lift Prediction Workshop (HLPW-3)⁴ were to assess the numerical prediction capability of current-generation CFD technology/codes for conventional high-lift configurations, to develop practical modeling guidelines for CFD prediction of high-lift flow fields, to determine the elements of high-lift flow physics that are critical for modeling to increase the accuracy of prediction methods and tools, and to enhance CFD prediction capability for practical high-lift aerodynamic design and optimization. Using well defined test cases, in terms of both geometry and flow conditions, the 1st and 2nd High Lift Prediction Workshops^{2,3} yielded meaningful comparisons between the participants that were able to highlight areas where the community as a whole required improvement. The 2nd High Lift Prediction Workshop HLPW-2 focused on one wing with an abundance of test data to use for comparisons (DLR-F11) for use as a verification case for the CFD tools. HLPW-3 increased the number of geometries to three with each one being used to highlight a certain portion of the whole CFD process. The workshop includes the High-Lift Common Research Model (HL-CRM)⁵ for a grid convergence study (Case 1), and the JAXA Standard Model (JSM)⁶ to compare with a large experimental database (Case 2), and the 2-D DSMA661 (Model A) airfoil from the Turbulence Modeling Resource (TMR)⁷ to verify the turbulence model implementation (Case 3).

In this work, the Launch Ascent and Vehicle Aerodynamics (LAVA)⁸ framework was used to solve the three workshop cases. The LAVA framework is currently under development at NASA Ames Research Center and the workshop provided an excellent opportunity to test the capabilities of the framework on highly complex geometries and flow fields. One of LAVA's features is that it supports the use of multiple mesh paradigms: structured Cartesian, structured curvilinear, and unstructured arbitrary polyhedral. For this work, the workshop problems are used to perform verification and validation studies of both the body-fitted mesh approaches within the LAVA framework (structured curvilinear and unstructured arbitrary polyhedral). Case 1 was used to perform a mesh refinement study to investigate the type of fidelity required within LAVA to properly capture the physics of these types of flows. Case 2 was used to validate both of the solvers against experimental data as well as to study the effects of using different turbulence model variations. Case 3 was used to validate the implementation of the SA model within both solvers. All of this data is summarized in this paper and used to develop a set of best practices for using LAVA to solve these types of problems.

III. Geometries and Test Cases

The workshop had three different test cases that had varying degrees of geometric complexity. The simplest of which was the 2D airfoil, then the NASA HL-CRM, and finally the JSM. The test case corresponding to each of these geometries was focused on one aspect of the CFD modeling problem. The geometries as well as the corresponding workshop test cases will be reported on in the following section in order of case number.

III.A. Case 1: High Lift Common Research Model

The first of the three test cases from the workshop is the HL-CRM. The HL-CRM, pictured in Fig. 1, is a wing-body with a high lift system in a nominal landing configuration (slat and flaps deployed at 30° and 37°, respectively) without nacelle, pylon, tails, or support brackets. The development of the HL-CRM was motivated by the success of the Common Research Model (CRM).⁹ The CRM has become a standard for both the experimental and CFD modeling communities where it represents a public domain, physically consistent geometry which has been used in numerous workshops and is currently a standard for a number of

experiments across the international community. The HL-CRM was developed by Boeing, as a representative high lift configuration based off of the existing CRM. Details of the various design criteria and geometry decisions can be found in the work done by Lacy and Sclafani.⁵

Case 1 involved performing a mesh refinement study on the HL-CRM at conditions that are representative of a wind tunnel test. The conditions for the case as well as some of the relevant physical parameters of the wing are provided in Table 1. The study was done to better understand the kind of mesh resolution that is needed to properly resolve the types of physics within this class of problems. In addition to performing the requested mesh refinement study in Case 1a, the effects of sealing some of the gaps on the geometry were also studied in Case 1c. Some of the areas where the gaps are sealed are shown in Fig. 2.

Quantity	Value
Mach Number	0.2
Alphas	8 and 16°
Reynolds Number based on MAC	3.26 Million
Reference Static Temperature	518.67°R (=15.00°C=59.00°F)
Reference Static Pressure	760.21 mmHg (=14.7 PSI)
MAC	275.8 inches full scale
Wing Semi-Span	1156.75 in
Reference Area for Semi-Span	297,360 in ²
MRC	X=1325.9 in, Y=468.75 in, Z=177.95 in

Table 1: HL-CRM Reference Quantities

III.B. Case 2: JAXA Standard Model

The second test case for the workshop was the JSM. The JSM was designed to be representative of a typical 100-person class regional airliner with a modern high-lift system (slat and flap deployed at 25° and 35°, respectively). This geometry was designed to be as representative of a real aircraft as possible, so it includes details such as a flow-through nacelle, flap track fairings, and slat attachment brackets. The experimental model was designed to have a removeable nacelle and pylon. This allowed for both a nacelle/pylon off (Case 2a) and nacelle/pylon on (Case 2c) version of the geometry which is shown in Fig. 3. More details on the exact specifications of the model and the corresponding wind tunnel test campaign can be found in the work done by Yokokawa et al.⁶

In addition to being a very realistic representation of a high lift system, the JSM also has the benefit of having a large amount of high quality experimental data that is available for comparisons with CFD. The JSM was tested in the JAXA 6.5-m by 5.5-m low-speed wind tunnel (JAXA-LWT1) at a Reynolds number of approximately 1.93 million based on the MAC. The test was run with a “freestream” velocity of 60 m/s, which corresponds to a Mach number of approximately 0.172. The model did not have any specified transition devices so the flow was allowed to naturally transition from laminar to turbulent. Forces, moments, pressure coefficients, oil flow, and transition data were all provided to the workshop for comparison with the CFD data. Since this geometry had a configuration with and without a pylon/nacelle, it was used to study if the flow solvers could accurately predict the installation effects of the nacelle and pylon. The CFD simulations were run at the same conditions as the wind tunnel conditions. The exact conditions along with some of the relevant physical parameters are given in Table 2.

III.C. Case 3: 2D Airfoil

The third and final case in the workshop was a verification study on the 2D DSMA661 (Model A) airfoil (Fig. 4) from the TMR website. The run conditions for this case are shown in Table 3. This case was done to assess the convergence of the grids on an airfoil as well as to assess the behavior of the velocity and turbulent shear stresses in the near wake. The wake behavior is especially important in high lift configurations because the wakes from the upstream elements pass over and interact with the wakes produced by the downstream elements. The complex interactions of the wakes is critical to predicting the proper drag for these types of

Quantity	Value
Mach Number	0.172
Alphas	4.36, 10.47, 14.54, 18.58, 20.59, and 21.57°
Reynolds Number Based on MAC	1.93 Million
Reference Static Temperature	551.79°R (=33.40°C=92.12°F)
Reference Static Pressure	740.70 mmHg (=14.458 PSI)
MAC	529.2 mm
Wing Semi-Span	2300 mm
Reference Area for Semi-Span	1,123,300 mm ²
MRC	X=2375.7 mm, Y=0.0 mm, Z=0.0 mm

Table 2: JSM Reference Quantities

configurations. This case was also used to verify the implementation of the turbulence model within the solver.

Quantity	Value
Mach Number	0.088
Alpha	0°
Reynolds Number Based on chord	1.2 Million
Reference Static Temperature	540°R

Table 3: 2D Airfoil Reference Quantities

IV. Flow Solver and Methodologies

The LAVA solver framework is utilized for this study. LAVA offers highly flexible meshing options and was developed with the intent of modeling highly complex geometry and flow-fields. The framework, shown in Fig. 5, supports Cartesian and curvilinear structured grids as well as unstructured arbitrary polyhedral meshes. For this work the curvilinear structured and arbitrary polyhedral mesh paradigms were utilized. Both the unstructured and structured modules solve the compressible Reynolds Averaged Navier Stokes (RANS) equations. In the structured module, the RANS equations are solved using a finite-difference formulation applied to the curvilinear transformed system of equations. Finite differencing was performed using the 2nd order modified Roe scheme with the Van Albada limiter. The unstructured module uses a 2nd order finite-volume discretization, with the data at the cell centers, using the AUSMPW+ convective flux discretization¹⁰ and a custom modified min/mod limiter. For this work, the Spallart-Allmaras (SA)¹¹ turbulence model was utilized with the Rotational Correction (RC)¹² and Quadratic Constitutive Relation.¹³ The f_{t2} term was not used for this work because it is intended to improve the prediction of transition within the SA model, but all of the cases were run fully turbulent. For the purposes of this paper “SA-noft2” will be shortened to simply “SA”.

All of the cases presented in this work were run on the Pleiades supercomputer at NASA Ames using a non-time accurate mode and assuming fully turbulent flow over the aircraft. All of the simulations were run at a fixed Courant-Friedrichs-Lewy (CFL) number and were considered converged when the standard deviation of the drag coefficient was within 0.00001.

Two types of free-stream initializations were used throughout this study, cold starts and warm starts. A cold start simply means that the whole flow field is initialized to the freestream condition. This is akin to the model being placed at an angle within the tunnel and then turning the tunnel on, with it instantaneously being at speed. A warm start means that the flow field of the simulation is initialized using the solution from a previous angle of attack while the freestream conditions are set to reflect the new angle of attack. This is similar to having the tunnel turned on and then changing the angle of the model. The differences between these types of flow field initializations is demonstrated within.

V. Mesh Generation

V.A. Grids for Case 1

The HL-CRM was also chosen by the 1st AIAA Geometry and Mesh Generation Workshop (GMGW-1)¹⁴ to assess the current state-of-the art in geometry preprocessing and mesh generation technology and software as applied to aircraft and spacecraft systems. Issues associated with grid generation and flow solution in the presence of open and partially sealed geometric gaps between the inboard and outboard flaps, and between the inboard flap and side of body prompted both workshops to include cases to evaluate increments and effects on the required cases. The HL-CRM cases presented here were done only using the structured overset LAVA module. The committee provided grids (labeled A-HLCRM_ StrOverset_ ChimeraGridTools) were downloaded from the website along with their Chimera Components Connectivity Program (C3P)¹⁵ domain connectivity files. The grids were generated following the HLPW3 workshop guidelines and details of the surface modeling and volume grid generation are found in Chan,¹⁶ where there are extensive descriptions of the process for generating the grids.

During the course of performing the initial simulations of this case using the provided grids, a couple of issues affected the quality of the results. The first was an issue involving the manner in which the final surface mesh points are projected onto a fine triangulation representation of the geometry instead of to the CAD representation. More information on this issue can be found in the paper by Coder et al.¹⁷ The second issue was the order of some of the manual grid splitting of the slat grids. The slat surface grids were generated as a single, periodic mesh that was then manually split prior to the volume grids being generated. This caused some issues with the solution within the split regions. The effect of this type of splitting and its solution will be discussed within the section VI.B of this paper. The final version of the grids posted on the website, pictured in Fig. 6, and used within this study had fixed both of these issues. Some of the details of the final mesh family are shown in Table 4.

Grid	Nodes	Cells	Blocks
Coarse	24,059,957	23,097,216	72
Medium	65,423,213	63,537,195	72
Fine	189,285,377	185,201,725	76
X-fine	564,384,433	554,523,792	102
Sealed (Medium)	66,269,520	64,364,621	73

Table 4: HL-CRM Mesh Characteristics

V.B. Overset Structured Grids for Case 2

As part of the workshop committee, the authors of this work volunteered to generate the overset-structured meshes for both the nacelle/pylon on and nacelle/pylon off versions of the JSM geometry. The grids were generated by following the gridding guidelines for a medium mesh using the Chimera Grid Tools (CGT)¹⁸ package. The CGT grid generation scripting framework allows for components to be added and subtracted with relative ease. With this in mind, it was decided to generate the grids for Case 2a (nacelle/pylon off) first, since it was the simpler of the two geometries. Once this mesh had been generated, the same scripts could then be used as the basis for the generation of the Case 2c (nacelle/pylon on) grids. Between both cases, the grid scripts are exactly the same for the fuselage, wing, flap, slat attachment hardware, and flap attachment hardware. The remaining portions of the Case 2c geometry, including the slat, wing stub, nacelle, and pylon, were generated from new scripts. The surface grids for the two cases are shown in Fig. 7.

The overset meshes were generated using established best practices for using CGT. The first step in the grid generation process was to first load the Standard Exchange of Product (STEP) file provided by the workshop committee into the ANSA¹⁹ software package and use it to generate unstructured surface patches. These patches are then exported from ANSA in STereoLithogrpahy (STL) file format. These are then used to generate structured Plot3D (P3D) grids and unstructured reference triangulations. The advantage of using ANSA to produce the structured patches directly is that it cuts out much of the manual work involved in generating reference curves, redistributing the curves, and then generating the grid zone within CGT. By doing these zones in ANSA the only step that is needed within CGT is to do the redistribution of the

grid. The unstructured grids are used in the traditional CGT workflow where they are first used to generate reference curves. Those curves are then used to generate surface grids and finally those surface grids are projected back onto the original triangulation. Once the surface meshes are made, it took little time to generate the volume meshes using CGT.

Throughout the mesh generation process, great care was taken to ensure that the grid was generated within the guidelines provided by the workshop committee. There were only a few areas where it was decided to deviate from the workshop guidelines. The first was that the number of points at the trailing edges of the elements was increased to 25 instead of the specified 9. This was done because the meshes were generated with an O-mesh topology rather than a C-mesh, which means that more resolution was needed along the trailing edges to ensure that there was sufficient resolution in the wake region. The spanwise spacing at the root and the tip of the main elements was also specified to be 0.1% of the semispan. Instead of strictly enforcing this spacing parameter, the cell sizes of the meshes in the root and tip areas were driven by the cell sizes of neighboring meshes. For the grids near the root, the spacings were driven by the cell sizes of the collar meshes, and at the tip they were driven by the cell sizings of the tip cap meshes. The result of this was that in all cases the cell sizes on the final meshes were finer than the 0.1% semispan guideline. The last area where the generated grids did not strictly adhere to the gridding guidelines was in the regions of the wakes of the three main elements. The guidelines specified a region of constant spacing within the volume mesh coming off the surface to accurately capture the wake. Instead of using this method, it was decided to use separate wake meshes to capture the wakes. Originally it was planned to generate these wake meshes by running a case at 14° angle of attack and then using the streamlines of the wake in the simulation to generate a wake mesh. This angle was chosen because it was an average angle of attack for the alpha sweep that would be needed in the workshop. However, when this first version of the wake grid was used at another angle of attack, it was discovered that the wake grid was not properly covering the desired regions of the flow field. Fig. 8 shows that this is being caused by the large variance within the wake streamlines as a function of the angle of attack. To solve this problem, it was decided to use a more geometry-based method of generating the wake grids. This means that the wake grids for each element were created by generating a spline using the upper surface of the trailing element and the tangent line from the trailing edge of the preceding element. The grids consisted of a fine core that would be aligned with the spline created from the components and a region that would stretch from the core to a desired maximum cell size. As the grid moved further down the span of the element the stretched section of the grid would fan out to allow for more of the wake to be captured across all of the angles of attack. This resulted in the two wake grids shown in Fig. 9. The blue wake grid captures the wake coming from the slat over the wing, and the pink grid captures the wake coming from the wing and over the flap. These wakes were found to be reasonably accurate across the whole range of angles of attack covered by the workshop.

Once both meshes had been finalized they were then passed on to fellow committee member, who then used PEGASUS²⁰ to generate the domain connectivity. The grids were then posted to the workshop site (labeled A-JSM_StrOverset_Chimera_Grid_Tools). For the simulations in this work, the grids from the website were used but not the provided connectivity files. The Modified Implicit Hole Cutting (MIHC) routines within LAVA were used to perform the overset connectivity. This was done to verify that the MIHC routines would provide reasonable connectivity for a complex geometry.

V.C. Unstructured Grids for Case 2

A medium grid was generated for Case 2c for a code-to-code comparison with the LAVA curvilinear results. The preferred element type for use with the LAVA unstructured solver is arbitrary polyhedra. No mesh with this element type was provided by the workshop committee so a custom mesh had to be generated. The unstructured mesh generation shares the same first step as with the structured grids. Starting from the provided CAD geometry in STEP format, an initial unstructured triangular surface mesh was first generated in ANSA following the workshop and in-house gridding guidelines. The surface mesh was then exported in the STL format format to STAR-CCM+²¹ for volume gridding using prismatic layers from the body surface and a polyhedral core mesh. The thickness of the first prism layer is set to realize $y^+=1$ at the wall with a stretching ratio of 1.2 and 0.5 aspect ratio between the last layer and first polyhedral layer height. The surface grid includes 1.6 million polygons. The volume grid includes 69.9 million cells and 339.9 million faces. Fig. 10 shows a side view of the surface grid on the wing and nacelle and a streamwise section of the volume grid.

V.D. Grids for Case 3

The grids for Case 3 were downloaded directly from the TMR website for both the unstructured and structured mesh topologies. For the structured solver, the 2D PLOT3D mesh family was used (Fig. 4). Since the solver is unable to handle a purely 2D mesh, the grids downloaded from the website were converted into 3D meshes. To do this, the 2D slice was copied and translated in the positive and negative span directions. The resulting mesh consisted of three planes with the exact same 2D profile. Periodic boundary conditions were applied to the two new planes to simulate a truly 2D airfoil. For the unstructured solver, the provided CGNS grids were used without any modifications. The computation of the wall distance in the code was modified to account for the fact that the cells are not grown in parallel to the wall normal in these grids.

VI. Results

High-fidelity simulations of the workshop cases were performed to assess the capabilities of the LAVA framework. The results of these simulations will be presented in order of increasing fidelity: Case 3 will be first, followed by Case 1, and finally by Case 2. The results for Case 3 will focus on verifying that the SA turbulence model has been implemented correctly by comparing the LAVA data to the data posted on the TMR website. The Case 1 results will be used to show how some aspects of the mesh generation process can have significant effects on the resulting flow field and to show that the LAVA results converge as the mesh is refined. Finally Case 2 will be used to show the installation effects of the nacelle and pylon, investigate the differences caused by using the different turbulence model variants, and show the effects of using cold starts versus warm starts.

VI.A. Test Case 3

All participants in the workshop were requested to perform a turbulence model verification study in Case 3. The data produced from the LAVA simulations using both the structured and unstructured solvers is compared against the provided data from the TMR website. In order to be consistent with the website results, both solvers were run with the SA model without the RC or QCR2000 corrections included. Fig. 11 shows the lift and the drag convergence with mesh resolution for both structured and unstructured LAVA solvers as well as the CFL3D and FUN3D data from the TMR website. To be considered "verified", the grid-converged lift and drag coefficients for a solver should fall in the range of that predicted by CFL3D and FUN3D. Taking a closer look at the drag breakdown shows that the structured and unstructured solvers consistently predict pressure drag similar to the values produced by CFL3D and FUN3D, but the unstructured solver predicts approximately 1 drag count lower viscous drag than the other solvers, which is currently thought to be related to the non-normal cell growth at the wall in the grids and treatment options for deferred gradient correction in the code. This topic is under further investigation. Fig. 12 plots a comparison of the mean velocity and Reynolds shear-stress wake profiles between LAVA and experimental data from Nakayama. Comparing the computed profiles to the CFL3D and FUN3D results on the TMR website shows no difference in the accuracy of the RANS solvers. This test-case provides additional confidence in the correct implementation of the governing flow equations and the SA turbulence model.

VI.B. Test Case 1

For Case 1 of the workshop, it was required to perform a mesh refinement study on the HL-CRM. This was done to investigate the spacial accuracy of the solver, the amount of discretization error, and the sensitivity of the forces to the grid resolution. This study was performed using the structured curvilinear grid topology using the SA turbulence model without the RC and QCR2000 variants. The code was run in steady state mode and all of the simulations were started from free stream conditions.

When the initial results from the simulations were being analyzed, local solution decoupling was observed on the slat in the overlapping regions of the mesh. Fig. 13 shows how this decoupling looked across the coarse, medium, and fine mesh levels. When dealing with overset mesh topologies some solution decoupling at the grid interfaces is expected and it is normally caused by suboptimal overlap on the surface. When the interface responsible for producing this decoupling was inspected it was found that the surface mesh was perfectly point matched. This was because the surface of the slat had been generated as one periodic mesh which was then split into two pieces in the chord direction. When a slice was taken through the volume, shown in

Fig. 14(a), it revealed that the origin of the decoupling was not from the grid interface at the surface but rather from the location of the volume grid boundaries. Fig. 14(a) shows that the boundaries of two slat grids are located in very different places relative to the physical geometry. This is causing the two slat grids to be receiving information from two distinct portions of the flow field which, in turn, is causing the solution decoupling at the surface shown in Fig. 14(b). The decoupling in Fig. 14(b) is happening at both overset interfaces between the two slat grids, but is much worse in the cove region. This is due to the fact that the difference in the location of the grid boundaries is much worse in the cove region than along the upper surface of the slat. This grid topology was a result of how the meshes were generated. While the surfaces were generated from the exact same mesh, as described earlier, the volume grids were made completely independently. This means that both grids were allowed to splay across one another. The only requirement was that there was sufficient point overlap between the resulting volume meshes.

The remedy for this gridding issue was to simply change how the mesh was split into two pieces. Instead of splitting the surfaces of the mesh, the volume mesh was first generated as one periodic grid. Once this grid was made, it was then split into the two final grids that were point matched along the whole mesh interface. Fig. 15(a), which is the same exact slice as in Fig. 14, shows how this results in two grids that are point matched along the entirety of the grid interface in the volume as well as along the surface. The resulting C_P distribution in Fig. 15(b) shows that the solution decoupling is eliminated entirely in the upper surface region of the slat and almost entirely in the cove region. The changes in mesh topology were implemented into the final version of the HL-CRM grids that were posted to the workshop website.

The final version of the workshop grids were then used to perform a mesh refinement study. These cases were all run using the steady state mode within LAVA and assumed that the flow was fully turbulent. The SA model was used as the turbulence model for all of these cases. In addition to assuming fully turbulent flow, the cases were all initialized from free stream and not restarted from lower angles of attack. Fig. 16 shows the resulting lift and drag forces for both 8 and 16° angle of attack plotted against the size of the mesh. For both angles of attack, the lift curve appears to be trending towards a converged value. The drag seems to be trending towards a converged value for the 16° case but not for the 8° case based on the changes in the slopes between each mesh level. Besides the anomalous behaviour of the drag on the extra fine mesh at 8°, the results seem to show that both the lift and drag are converging as the mesh is refined. From these results the fine mesh is the recommended level for this type of problem. The complexity of these types of flows, especially at the higher angles of attack, necessitates the use of a large amount of points to fully resolve the relevant flow features.

VI.C. Test Case 2

Case 2 of the workshop was used to assess the capabilities of the LAVA framework for prediction of the performance of high lift systems. To perform this assessment, the curvilinear solver was used to simulate both the nacelle/pylon off (2a) and on (2c) configurations and the unstructured solver was used to simulate the nacelle/pylon on configuration. The nacelle/pylon installation study was done within the curvilinear solver to assess the predictive capabilities of the solver using current best practices. The structured solver was also used to investigate the effects of the flow field initialization as well as the turbulence modeling effects. The unstructured solver was only run on Case 2c. It was run using the same best practices that were used for the structured solver to assess their performance against one another.

The established best practices for high lift problems meant that the cases were run in the steady-state mode, utilizing the SA turbulence model, and with the flow field initialized to the free stream quantities. The individual cases were considered converged once the oscillations within the standard deviation of the loads had been reduced as much as possible. The target criterion was to have the standard deviation of the drag to be within a tenth of a drag count when averaged over the last 1000 iterations. Due to the unsteady nature of the flow at the higher angles of attack, some cases were considered converged when the standard deviation of the drag did not change in magnitude when averaged over a window of 1, 5, and 10 thousand iterations. The resulting lift and drag curves for Case 2a and 2c are shown in Fig. 17 and 18. In both cases, the lift is slightly under predicted at the lower angles of attack (4.36, 10.47, and 14.54°) and is significantly under predicted at the higher angles of attack (18.58, 20.59, and 21.57°). It also appears that LAVA is predicting stall between 14.45 and 18.58° angle of attack, which is much earlier than in the experiment. While the lift is being under predicted the drag is over predicted across the whole angle of attack sweep. The disagreement between the LAVA solution and the experiment is worse at the higher angles of attack. All of the issues that are seen at the higher angles of attack, in both the lift and the drag, are due to the flow separation not being

properly predicted. Two areas where it was clear that improvements could be made were the initialization of the flow field and the fidelity of the turbulence modeling.

The flow field initialization was identified as an area of improvement because the approach that was used in the simulations was not matched to how the case was run in the experiment. Initializing the flow field to be free stream everywhere is equivalent to putting the model at the desired angle of attack and then running the tunnel. When the test was performed, the model was placed at an initial angle of attack and then rotated while the tunnel was still on. To be more representative of this type of physical transient, the flow field for the higher angle of attack cases was initialized using the solution from the previous angle of attack. Since there was good agreement between the simulation and the experiment at the low angles of attack it was decided to only alter the flow field initialization for the high alpha cases. The resulting lift and drag curves for Case 2a and 2c are shown in Fig. 19 and 20 respectively. For both configurations, the lift and drag predictions are trending towards the experimental results. For Case 2a, the lift does not show any stall up to 21.57° while in Case 2c the stall is predicted to be between 20.59 and 21.57° . Though this change does improve the agreement between the LAVA and experimental data it does not account for all of the difference between the two.

From previous workshops, it is well established that the turbulence model can have a large effect on the predicted flow field, especially at high angles of attack. Prior to this work, the SA model had been implemented into LAVA without any corrections. It was decided to implement both the RC and QCR2000 corrections to the solver because these had been shown to improve the predictions of flow solvers in the HLPW2 results. Fig. 21 shows the lift and drag curves for Case 2c with all of the turbulence model perturbations. The SA-QCR2000 result shows that the correction has reduced the amount of lift predicted at the lower angles of attack, but that the flow has stayed attached up to 18.58° . It has also slightly reduced the amount of predicted drag as compared to the SA result. The SA-RC increases the predicted lift across the whole alpha sweep and the predicted stall angle is between 20.58 and 21.57° . On the drag curve the SA-RC correction has increased the drag at 10.47 and 14.45° while reducing the drag predicted at the three highest alphas relative to the SA result. When both the RC and QCR2000 corrections are included, the lift increases towards the experiment at the three lowest angles of attack, but not as much as the SA-RC result. The inclusion of both the corrections produces drag values similar to only having RC included. The largest difference between the SA-RC and SA-RC-QCR2000 is in the moment predictions (Fig. 20(c)). The SA-RC variant is doing the best job of predicting the moment over the whole alpha sweep.

The differences in the force and moment curves in Fig. 20 are due to the different model variants predicting different separation patterns over the geometry, as shown in Fig. 22. The area where the different corrections are having the most effect on the solution is along the outboard section of the wing, specifically the area behind the two outermost slat attachment brackets. The large drop in lift that is seen in the SA curve in Fig. 20 is being caused by the large separation region behind the fourth outermost slat bracket. All of the other variants do not show that same separation pattern. Of the three corrected variants, the SA-RC (Fig. 22(b)) predicts the smallest separation near the wing tip region while the SA-QCR2000 (Fig. 22(c)) shows the largest. This explains the differences in the lift and drag curves from Fig. 20. It is important to note that while all of the different variants of the SA model show different separation, none of them are predicting exactly the same separation as the experiment. Fig. 23 shows the comparison between the SA-RC-QCR2000 result from LAVA to an oilflow image from the experiment. It clearly shows that the CFD is not predicting the same separation pattern. The differences between the two images can be largely attributed to transitional effects. In the experiment the flow was allowed to naturally transition while in the CFD the flow was forced to be fully turbulent. To accurately simulate the experiment would require the inclusion of a transition model within LAVA. However, since there is no transition model currently implemented within LAVA, it is recommended that the SA-RC-QCR2000 turbulence model be used for this type of problem.

Both the corrections included in the turbulence model and the method of flow field initialization have been shown to have significant effects on the solver's predictions at the high angles of attack. Including both the RC and QCR2000 in the turbulence model showed improvements in predictions. Additionally utilizing warm starts with the standard SA model showed improvement in the predictions, but when both were applied simultaneously the predictions did not improve, as shown in Fig. 24. It requires further investigation to understand why warm starting with RC and QCR2000 does not improve the predictions.

Case 2c was also used to compare the unstructured and structured solvers against one another. Fig. 25 shows the lift and drag curves produced from both solvers. These particular simulations utilized the SA-RC-QCR2000 turbulence model and with warm starts. Both solvers compare well to one another in the linear

regime prior to stall. Post stall both solvers behave slightly differently but in both cases the lift is under predicted and the drag is over predicted. This case was intended to be a spot check of the unstructured solver and, to that end, the comparison between the two mesh topologies is encouraging.

VII. Summary

All three cases from the HLPW3 were run using the LAVA framework. Case 3 was used to verify that the SA turbulence model had been properly implemented into both the curvilinear and unstructured solvers within LAVA by comparing the LAVA data to the data from the TMR website. The mesh refinement study for Case 1 was performed using the curvilinear solver and the effects of refining the mesh on the predicted aerodynamic loads were discussed. Case 2 was used to show that both the unstructured and structured solvers produce similar results before stall when they are run using the same models. The Case 2 results demonstrated the effects of using different flow field initialization strategies and SA turbulence model variants on the predictions from the LAVA curvilinear solver.

The improvements in the Case 2 results are significant but there is still room for more to be made. One major improvement that is currently being developed is a transition model. This is especially important to this case because, the flow was allowed to naturally transition in the experiment. At the higher angles of attack the flow field becomes more unsteady. This unsteadiness can be more accurately captured through the use of a hybrid Reynolds Averaged Navier-Stokes/Large Eddy Simulation or Wall Modeled-Large Eddy Simulation method. These methods are currently under development within LAVA.

VIII. Acknowledgments

The authors appreciate the support of the Transformative, Tools, and Technology (T³) project under NASA's ARMD Transformative Aeronautics Concepts Program (TACP). The authors would like to thank the organizing committee for the 3rd AIAA High Lift Prediction Workshop for organizing and hosting the workshop. The authors are also appreciative of the work done by the Geometry and Mesh Generation Workshop to mesh the HL-CRM, specifically William Chan for his work on generating the overset meshes that were used in this work. The authors would like to thank Jeff Slotnick for providing feedback on the wake grids that were used in the structured grid system as well as for his work in generating the PEGASUS5 connectivity files for the grids. The authors would also like to thank Tom Pulliam for valueable discussions throughout the process of running and post processing the workshop cases. Computer time was provided by NASA's Advanced Supercomputing (NAS) facility at NASA Ames Research Center

References

- ¹Tinoco, E., Brodersen, O., Keye, S., and Laffin, K., "Summary of Data from the Sixth AIAA CFD Drag Prediction Workshop: CRM Case 2 to 5," *55th AIAA Aerospace Sciences Meeting*, January 2017, AIAA-2017-1208.
- ²Rumsey, C., Slotnick, J., Long, M., Stuever, R., and Wayman, T., "Summary of the First AIAA CFD High-Lift Prediction Workshop," *Journal of Aircraft*, Vol. 48, No. 6, 2011, pp. 2068–2079.
- ³Rumsey, C. and Slotnick, J., "Overview and Summary of the Second AIAA High Lift Prediction Workshop," AIAA 2014-0747, 52nd AIAA Aerospace Sciences meeting, National Harbor, Maryland, Jan. 2014.
- ⁴Rumsey, C. and Slotnick, J., "Overview and Summary of the Third AIAA High Lift Prediction Workshop," AIAA TBD, 56th AIAA Aerospace Sciences meeting, Kissimmee, Florida, Jan. 2018.
- ⁵Lacy, D. S. and Sclafani, A. J., "Development of the High Lift Common Research Model (HL-CRM): A Representative High Lift Configuration for Transonic Transports," *54th AIAA Aerospace Sciences Meeting*, January 4-8 2016, AIAA-2016-0308.
- ⁶Yokokawa, Y., Murayama, M., Kanazaki, M., Murota, K., Ito, T., and Yamamoto, K., "Investigation and Improvement of High-Lift Aerodynamic Performances in Low-speed Wind Tunnel Testing," *46th AIAA Aerospace Sciences Meeting and Exhibit*, January 2008, AIAA-2008-0350.
- ⁷Rumsey, C., "Recent Developments on the Turbulence Modeling Resource Website (Invited)," AIAA 2015-2927, 22nd AIAA Computational Fluid Dynamics Conference, Dallas, Texas, 2015.
- ⁸Kiris, C., Housman, J., Barad, M., Brehm, C., Sozer, E., and Moni-Yeta, S., "Computational Framework for Launch, Ascent, and Vehicle Aerodynamics," *Aerospace Science and Technology*, Vol. 55, August 2016, pp. 189–219.
- ⁹Vassberg, J. C., Dehaan, M. A., Rivers, M., and Wahls, R. A., "Development of a Common Research Model for Applied CFD validation Studies," AIAA 2008-6919, 26th AIAA Applied Aerodynamics Conference, Honolulu, Hawaii, Aug. 2008.
- ¹⁰Kim, K. H., Kim, C., and Rho, O.-H., "Methods for the Accurate Computations of Hypersonic Flows: I. AUSMPW+ Scheme," *Journal of Computational Physics*, Vol. 174, November 2001, pp. 38–80.
- ¹¹Spalart, S. and Allmaras, S., "A One-Equation Turbulence Model for Aerodynamic Flows," *30th Aerospace Sciences Meeting and Exhibit, Reno, NV*, January 1992, AIAA-92-0439.

- ¹²Shur, M. L., Strelets, M. K., Travin, A. K., and Spalart, P. R., "Turbulence Modeling in Rotating and Curved Channels: Assessing the Spalart-Shur Correction," *AIAA Journal*, Vol. 38, No. 5, 2000, pp. 784–792.
- ¹³Spalart, P. R., "Strategies for Turbulence Modeling Simulations," *International Journal of Heat and Fluid Flow*, Vol. 21, 2000, pp. 252–263.
- ¹⁴Chawner, J. and Woeber, C., Geometry and Mesh Generation Workshop Website, <https://pointwise.com/gmgw>.
- ¹⁵Chan, W. M. and Pandya, S. A., "Advances in Distance-Based Hole Cuts on Overset Grids," *22nd AIAA Computational Fluid Dynamics Conference, AIAA AVIATION Forum*, June 22-26 2015, AIAA-2015-3425.
- ¹⁶Chan, W., "Best Practices on Overset Structured Mesh Generation for the High-Lift CRM Geometry," AIAA 2017-0362, 55th AIAA Aerospace Sciences Meeting, Grapevine, Texas, Jan. 2017.
- ¹⁷Coder, J. G., Puliam, T. H., and Jensen, J. C., "Contributions to HiLiftPW-3 Using Structured, Overset Grid Methods," *56th AIAA Aerospace Sciences Meeting*, January 8-12 2018, AIAA-2018-TBD.
- ¹⁸Chan, W., "Developments in Strategies and Software Tools for Overset Structured Grid Generation and Connectivity," *20th AIAA Computational Fluid Dynamics Conference, Honolulu, Hawaii*, June 2011, AIAA-2011-3051.
- ¹⁹BETA-CAE, ANSA Pre-Processing tool website, www.beta-cae.com/ansa.htm.
- ²⁰Suhs, N., Rogers, S., and Dietz, W., "PEGASUS 5: An Automated Pre-Processor for Overset-Grid CFD," *32nd AIAA Fluid Dynamics Conference and Exhibit, Fluid Dynamics and Co-located Conferences*, June 24-26 2002, AIAA-2002-3186.
- ²¹Siemens, STARCCM+ website, www.cd-adapco.com/products/star-ccm.

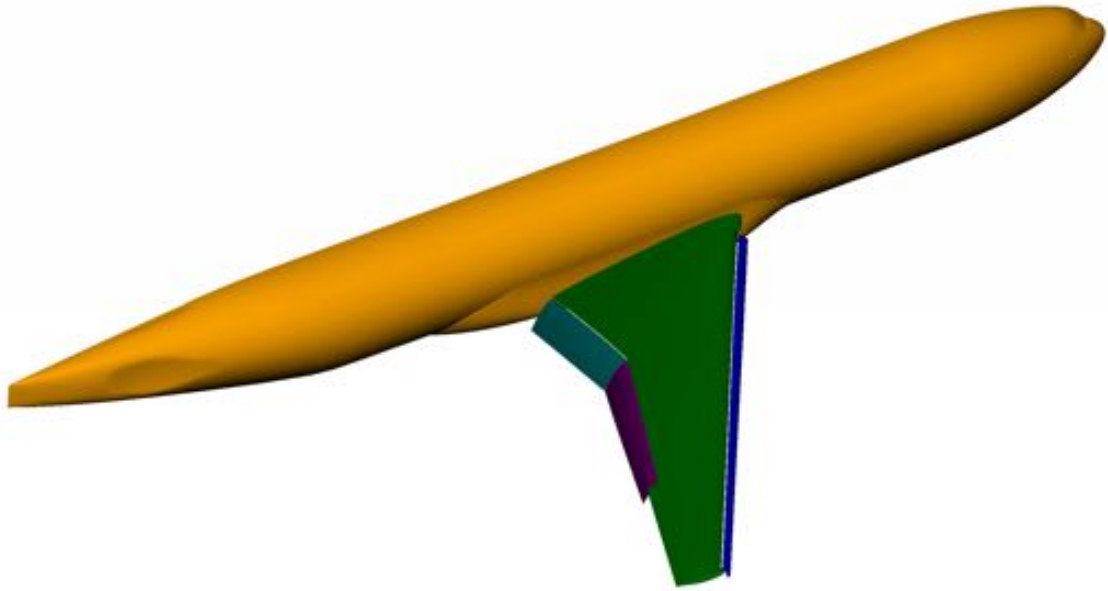


Figure 1: Perspective view of the HL-CRM geometry.

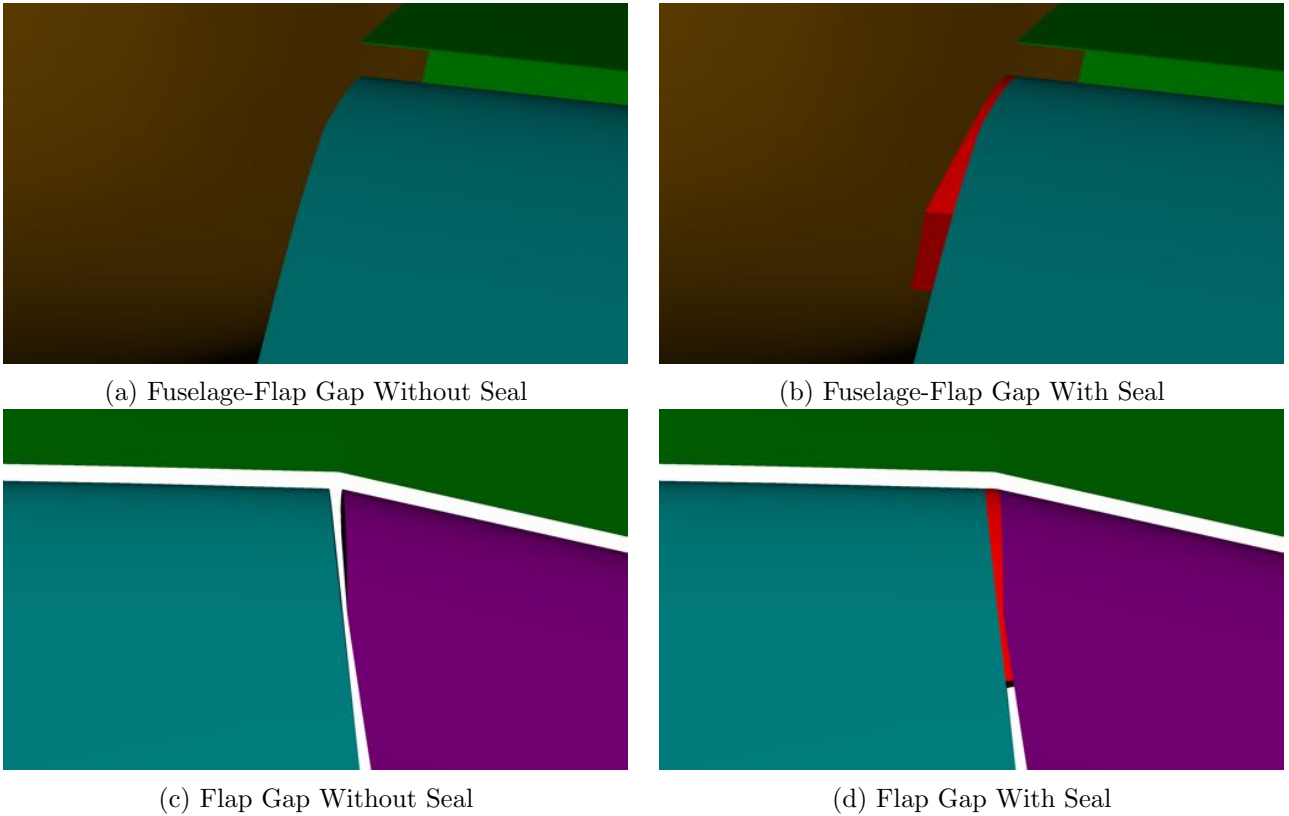


Figure 2: Zoomed in view in on the area between the inboard flap and the fuselage to show what it looks like in the (a) gapped and (b) sealed configurations. Zoomed in view in on the area between the inboard and outboard flaps to show the (a) gapped and (b) sealed configurations.



(a) Nacelle/Pylon Off



(b) Nacelle/Pylon On

Figure 3: Comparison of the (a) nacelle/pylon off and (b) nacelle/pylon on while installed in the tunnel for the JSM.

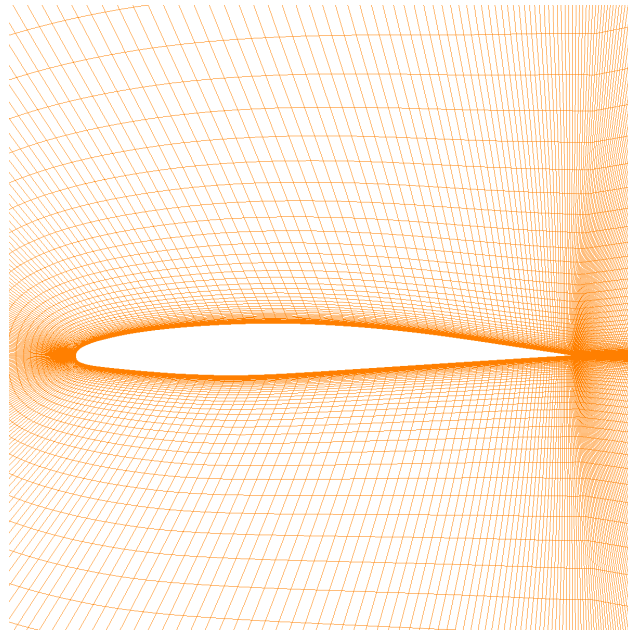


Figure 4: Airfoil Grid from TMR Website.

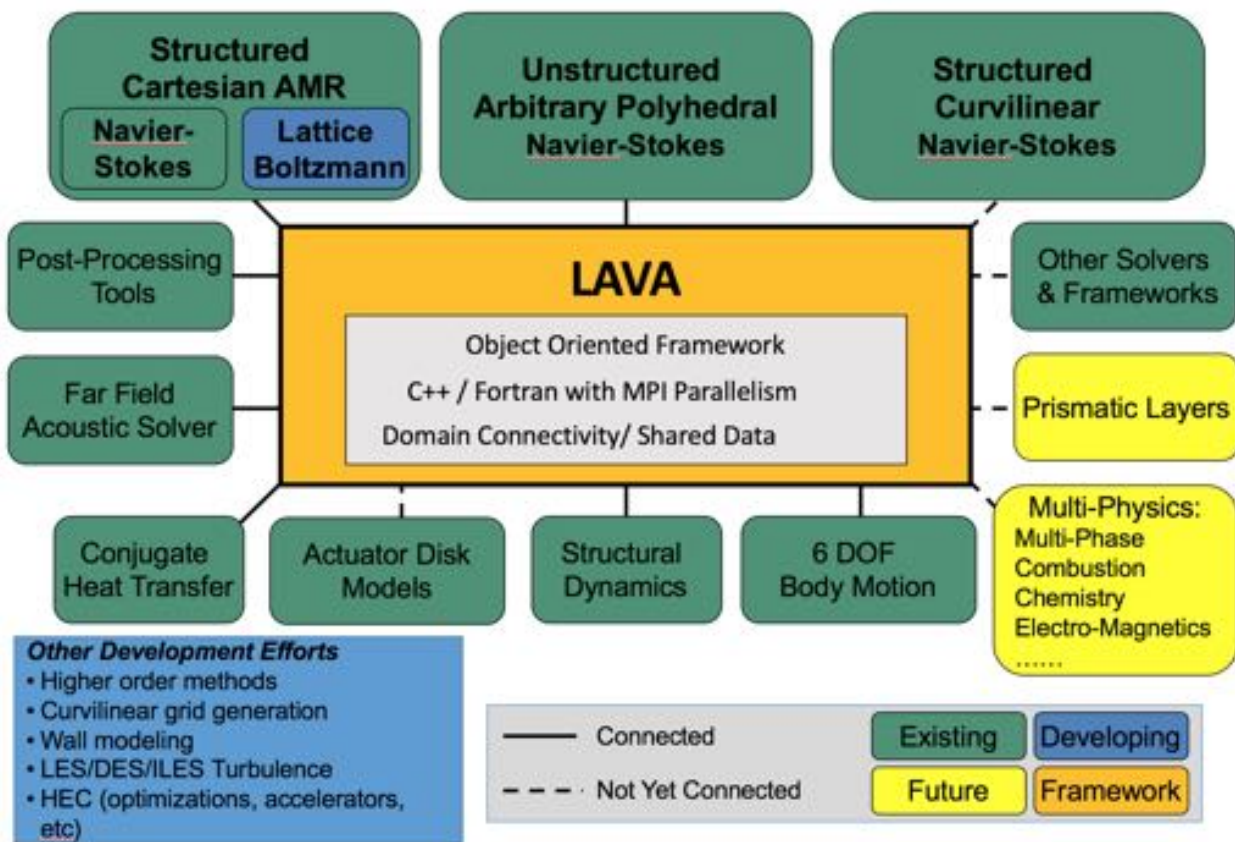
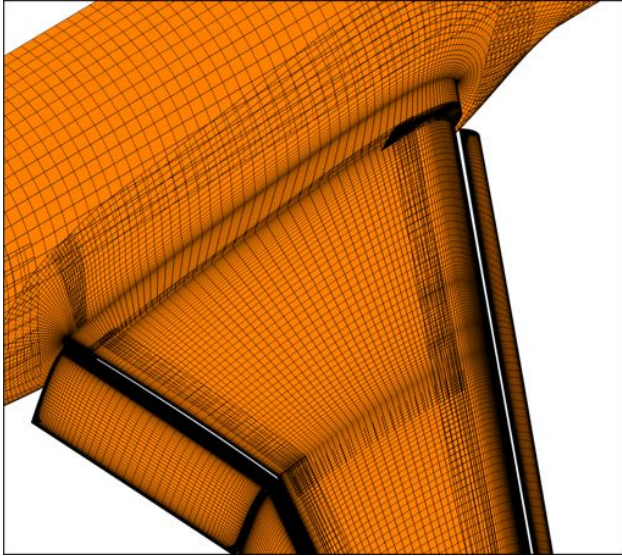
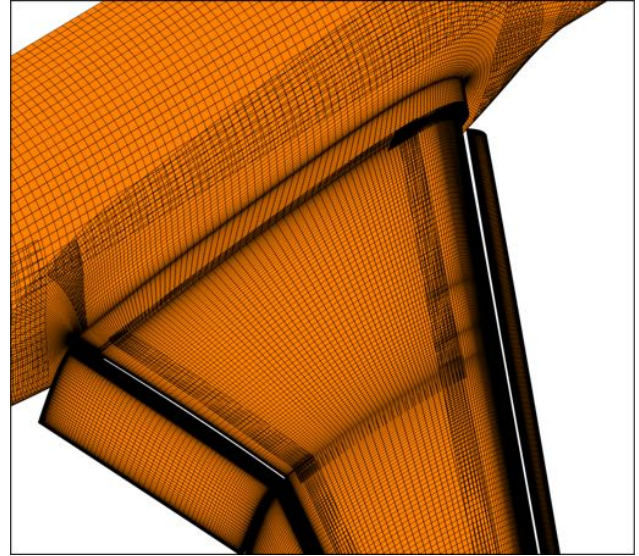


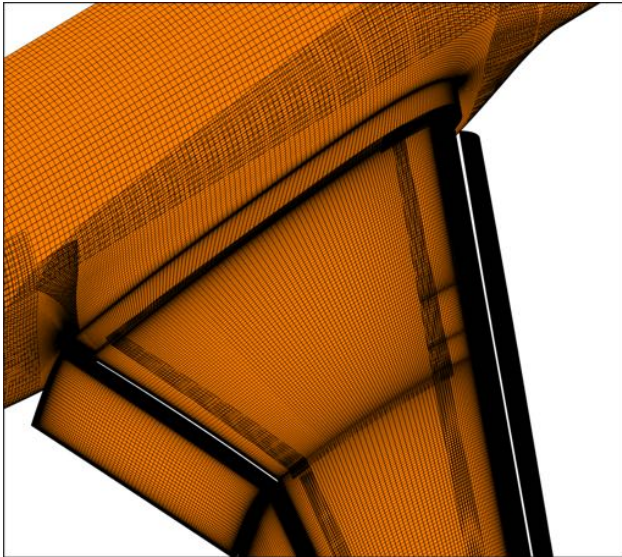
Figure 5: Schematic of LAVA infrastructure design illustrating current and future features.



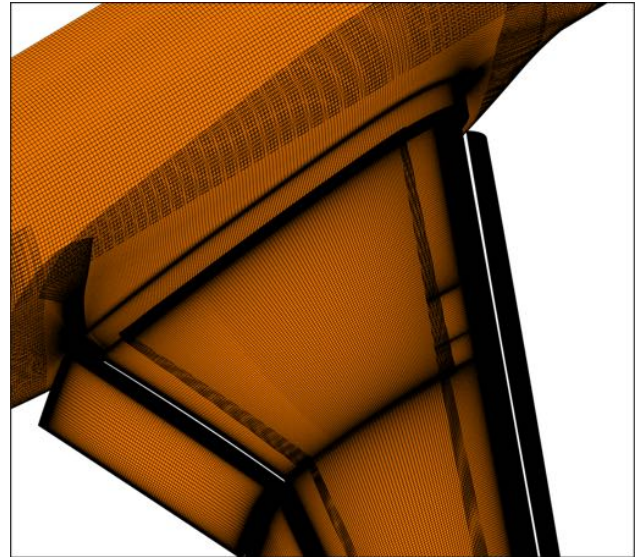
(a) Coarse (24M)



(b) Medium (65M)

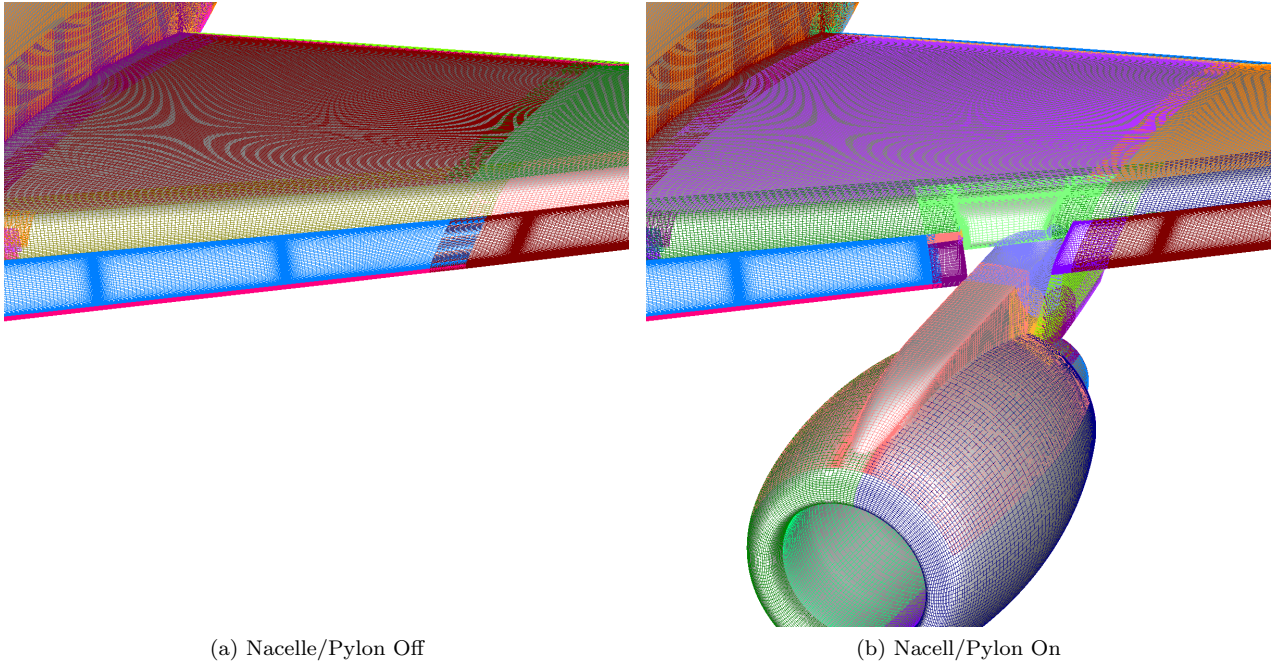


(c) Fine (189M)



(d) X-Fine (564M)

Figure 6: Isometric view of the HL-CRM showing the different mesh refinements, (a) coarse, (b) medium, (c) fine, and (d) extra fine.



(a) Nacelle/Pylon Off (b) Nacell/Pylon On
 Figure 7: Final mesh topology for the JSM overset surface meshes. (a) Case 2a. (b) Case 2c.

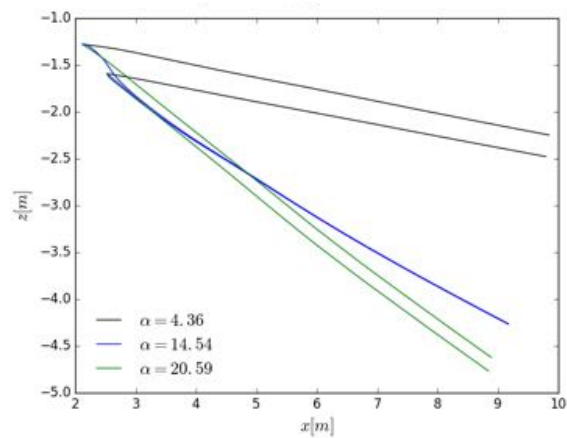


Figure 8: Wake streamlines at various angles of attack.

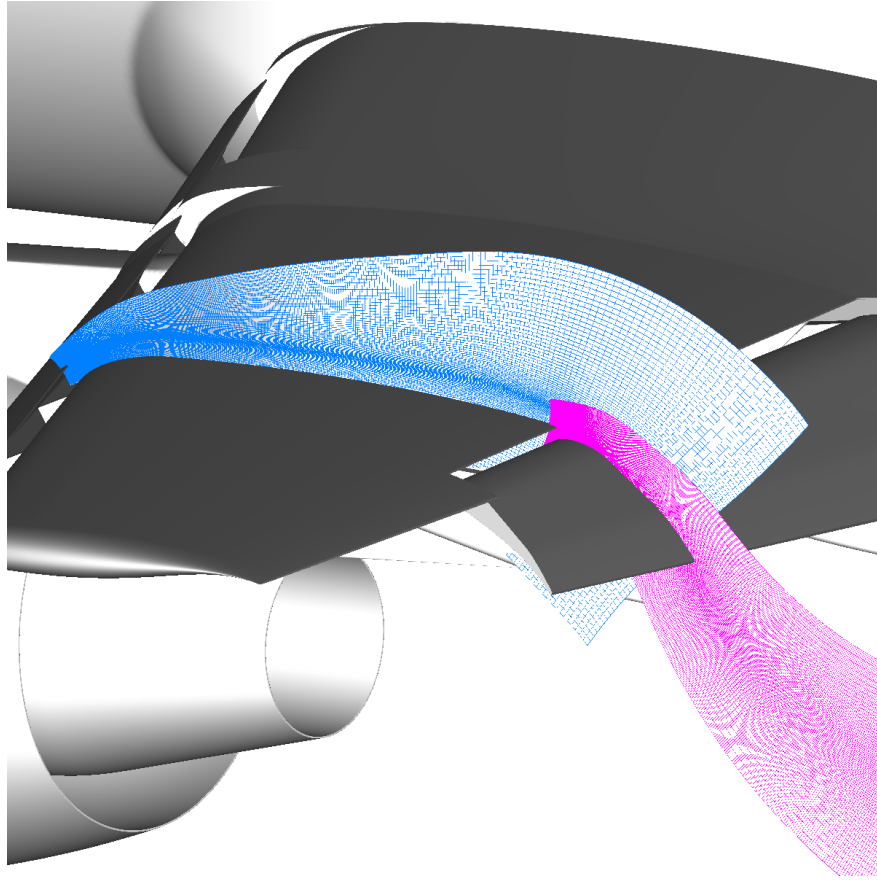


Figure 9: Final geometric wake grids for the JSM that are used at all angles of attack.

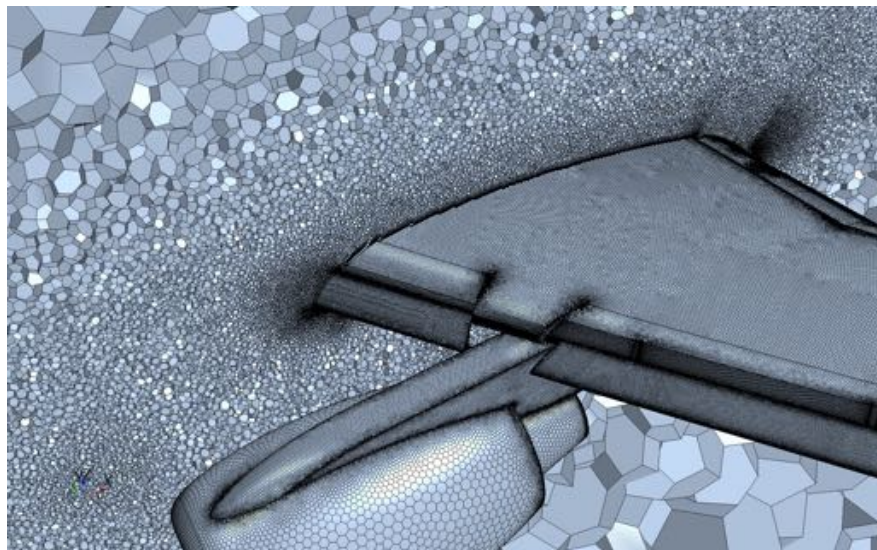


Figure 10: Slice through unstructured polyhedral mesh for the JSM.

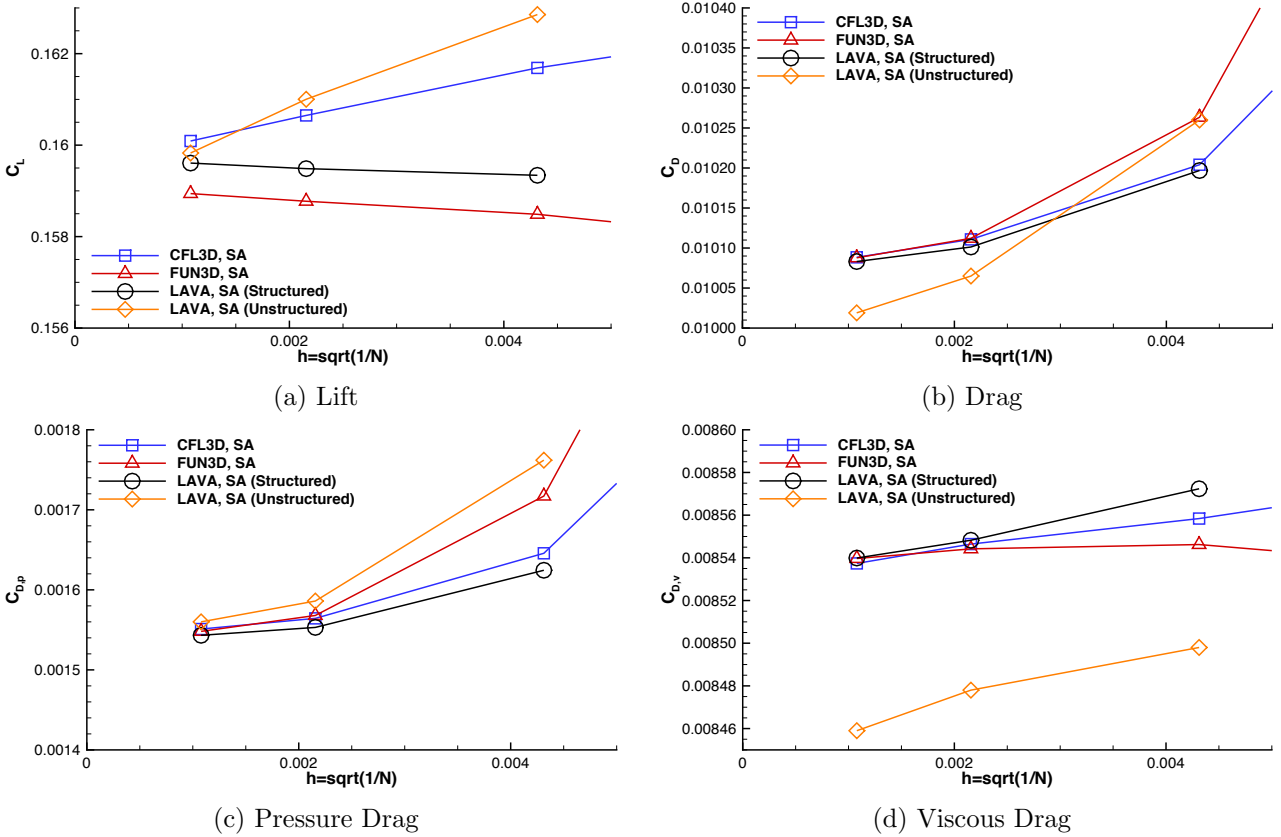


Figure 11: Comparison of lift and drag coefficient along with drag breakdown between LAVA, CFL3D, and FUN3D for Case 3.

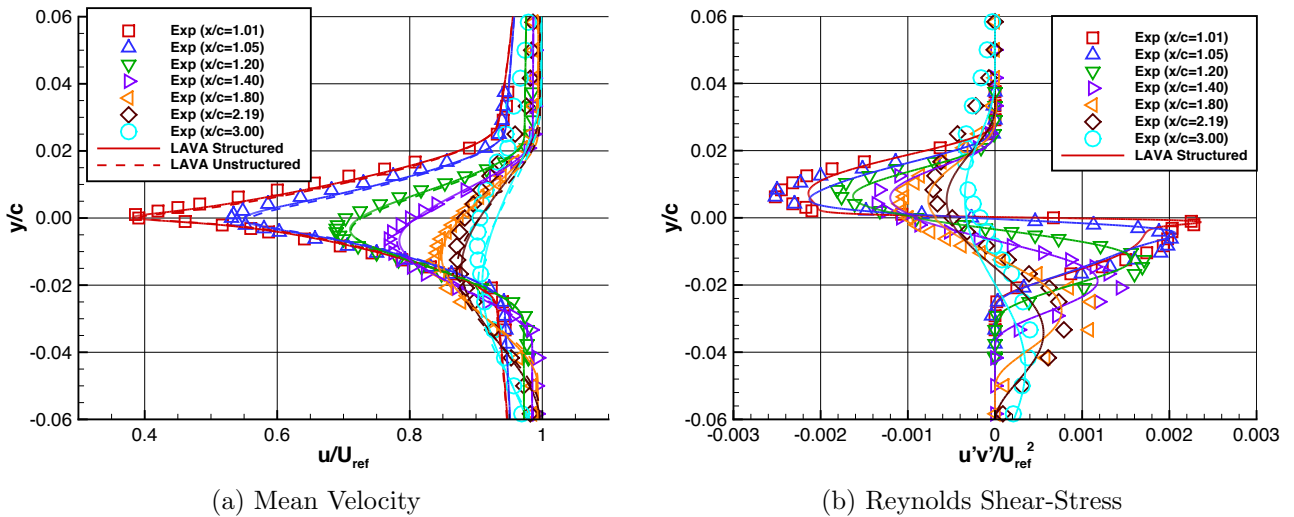
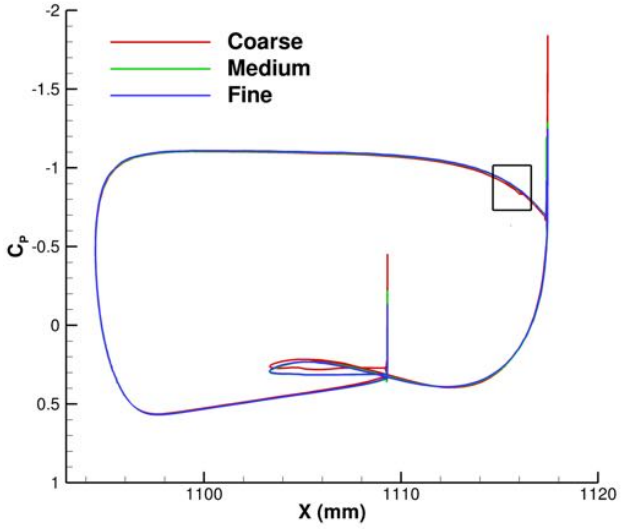
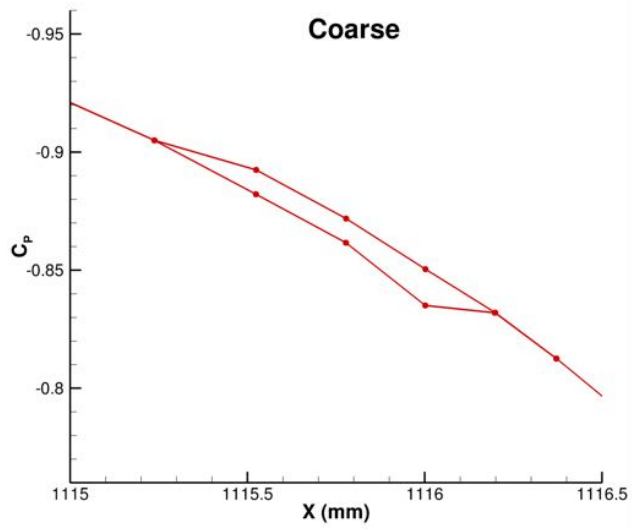


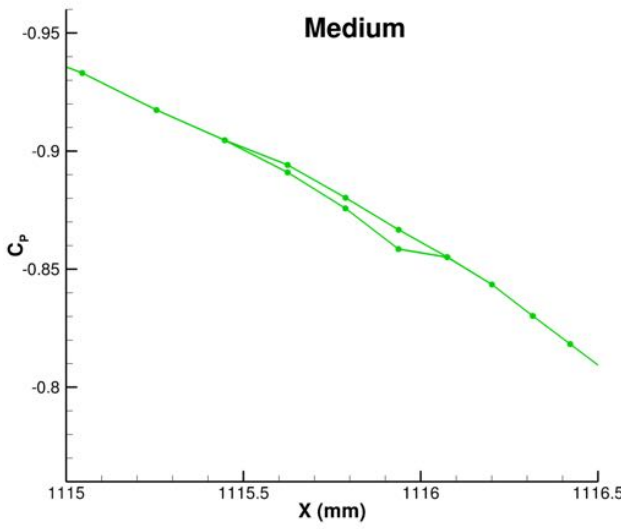
Figure 12: Comparison of (a) mean velocity and (b) Reynolds shear-stress wake profiles between LAVA and experimental data from Nakayama.



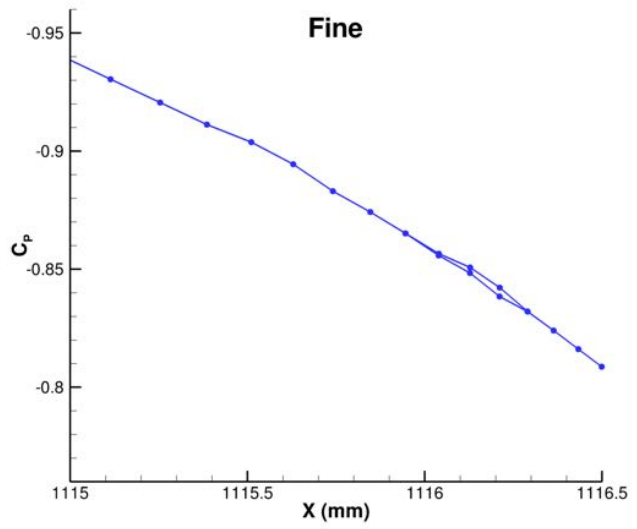
(a) Slat C_P Comparison



(b) Coarse Grid

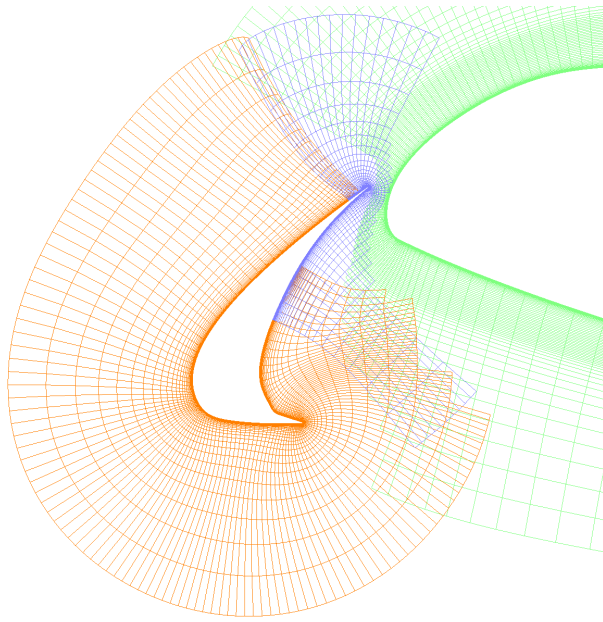


(c) Medium Grid

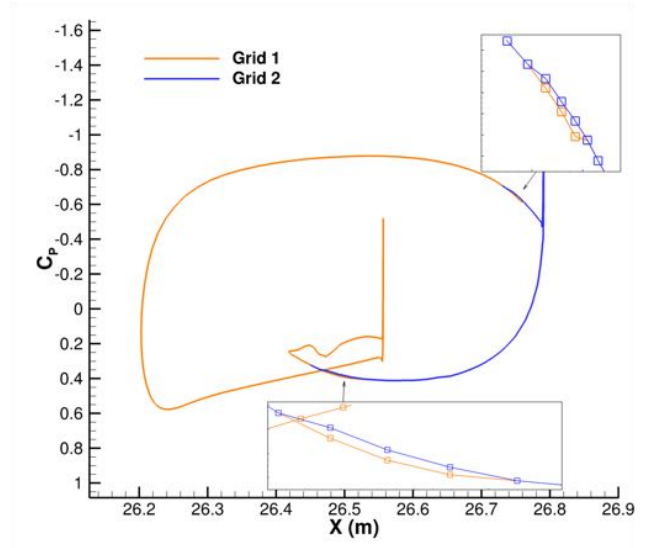


(d) Fine Grid

Figure 13: (a) C_P slice through a representative section of the HL-CRM slat showing local solution decoupling at the overset mesh interfaces across all of the grid levels. Zoomed in views on the decoupling for the (b) coarse, (c) medium, and (d) fine grids.

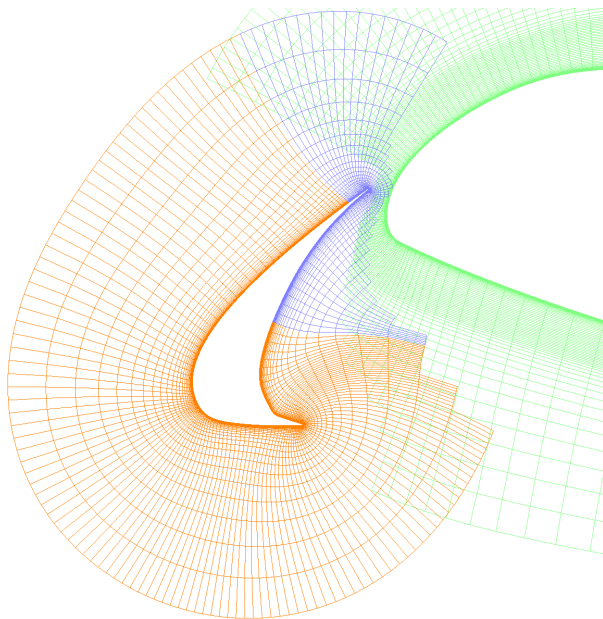


(a) Original Mesh

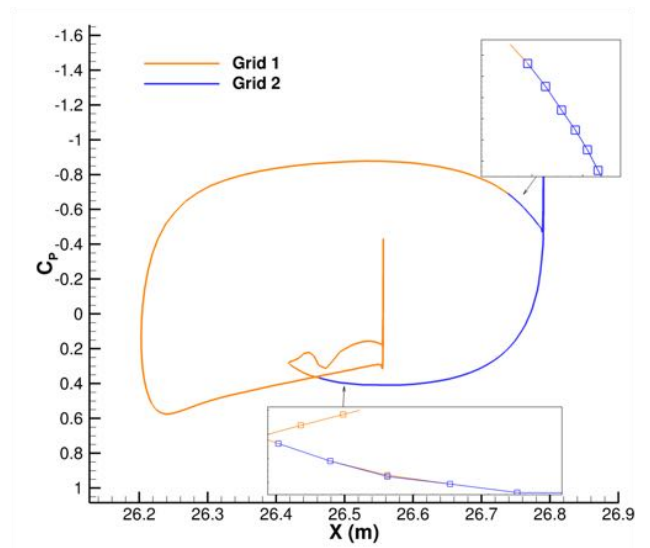


(b) Original C_P

Figure 14: (a) Slice through the original HL-CRM slat grid system and (b) its corresponding surface C_P plot.

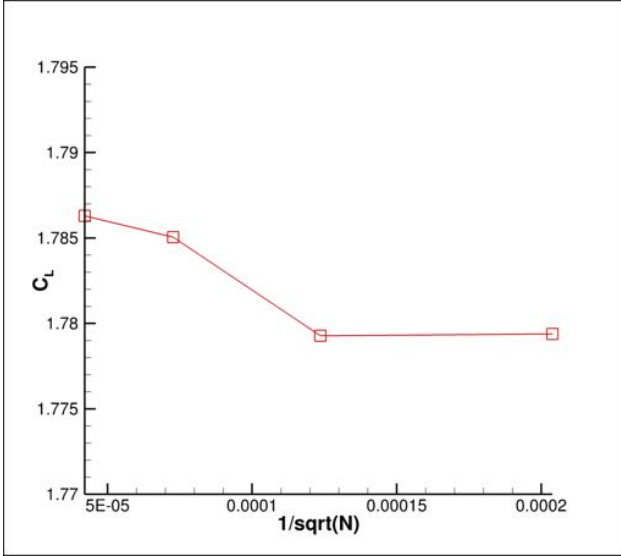


(a) Final Mesh

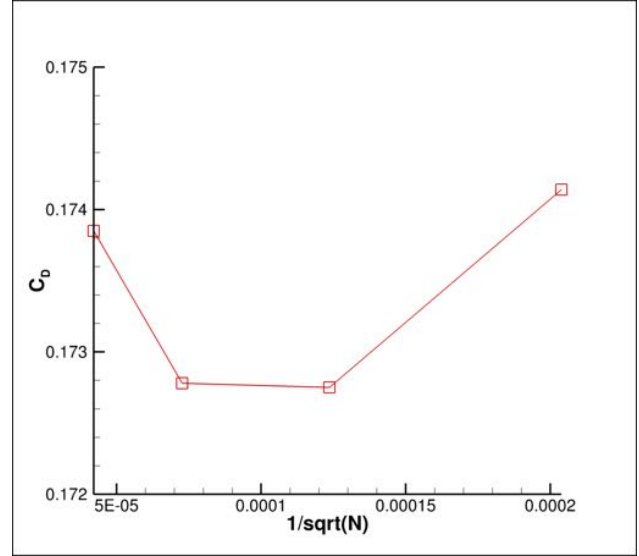


(b) Final C_P

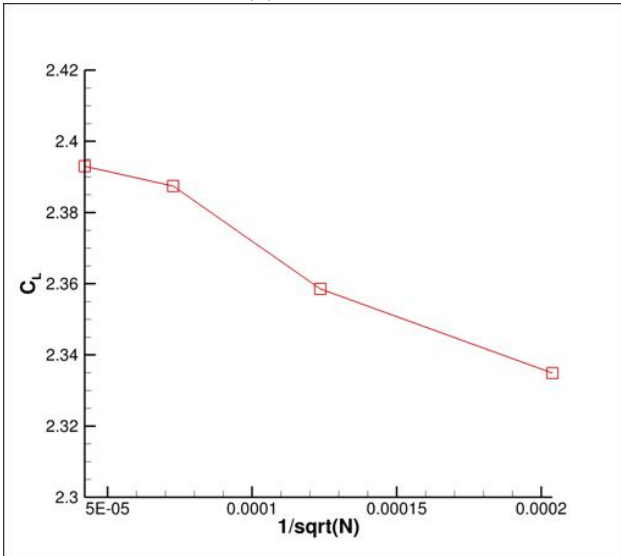
Figure 15: (a) Slice through the final HL-CRM slat grid system and (b) its corresponding surface C_P plot.



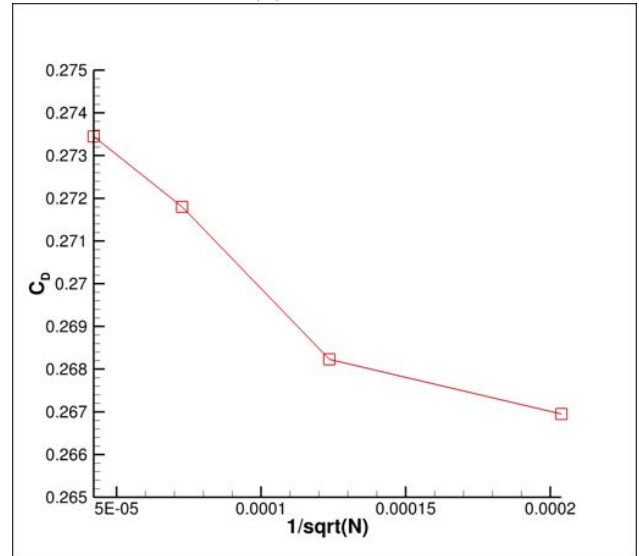
(a) C_L at 8°



(b) C_D at 8°

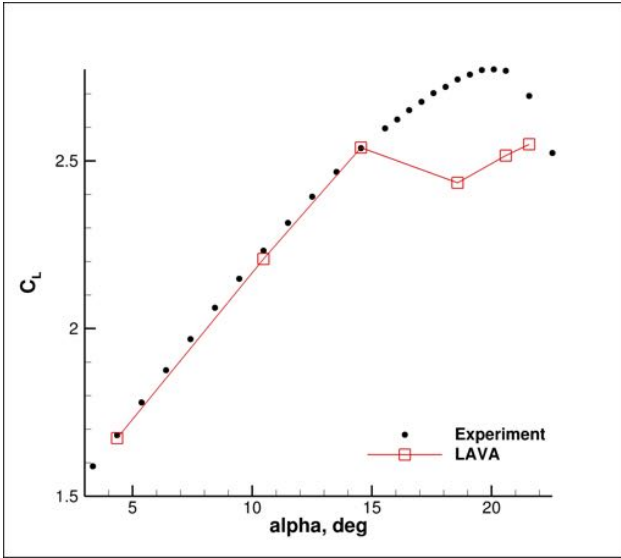


(c) C_L at 16°

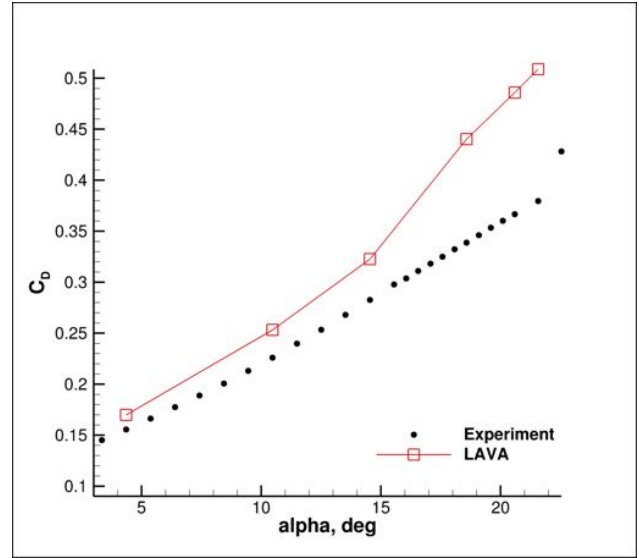


(d) C_D at 16°

Figure 16: Plots of the various forces for the mesh refinement study on the HL-CRM (Case 1).

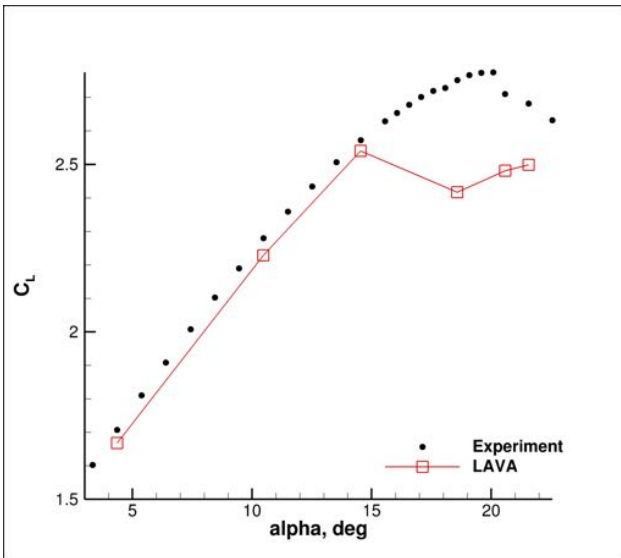


(a) Lift

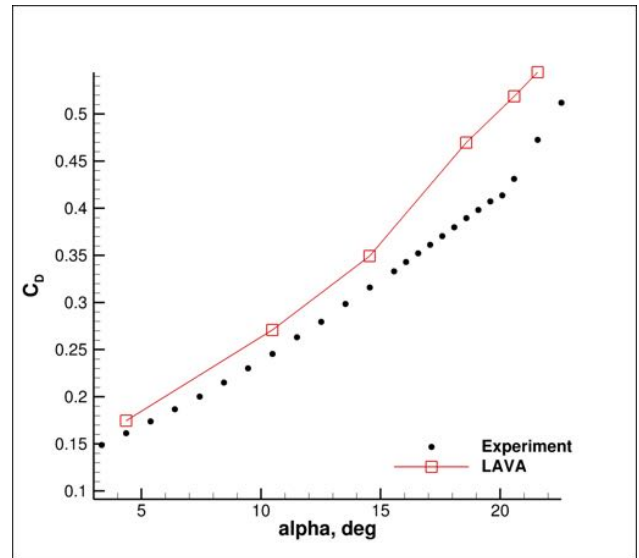


(b) Drag

Figure 17: Lift and Drag plots for the JSM without the nacelle/pylon (Case 2a).

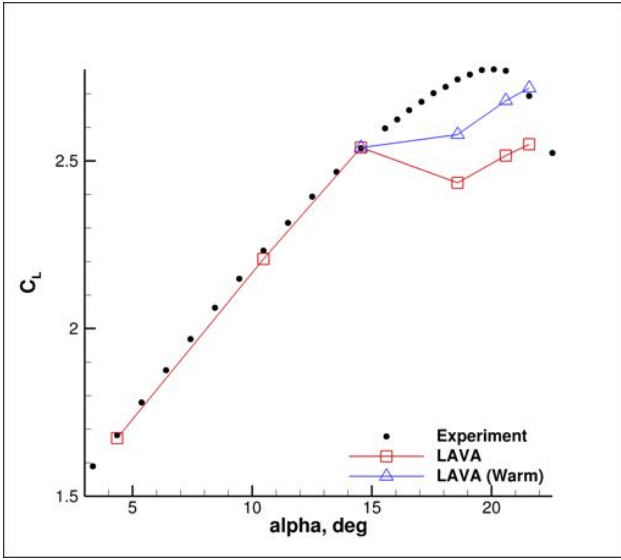


(a) Lift

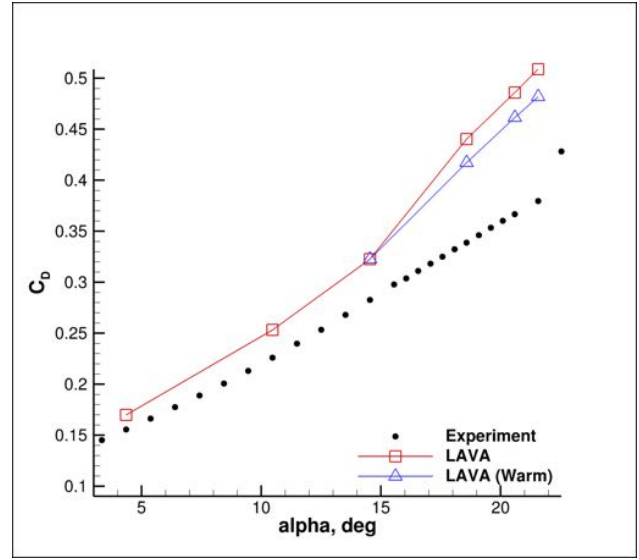


(b) Drag

Figure 18: Plots of the forces and moments for the JSM with nacelle/pylon installed (Case 2c).

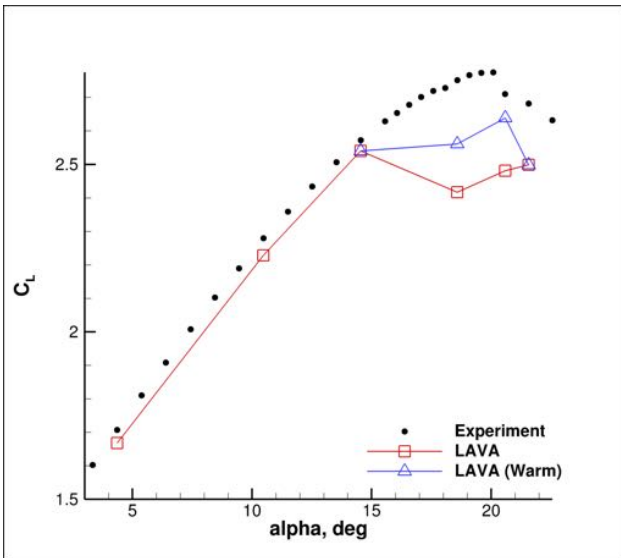


(a) Lift

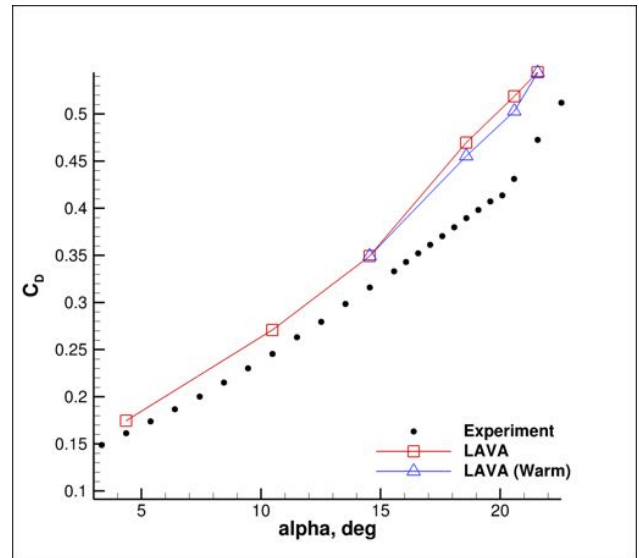


(b) Drag

Figure 19: Lift and drag plots for JSM Case 2a showing the difference between the cold and warm starts.

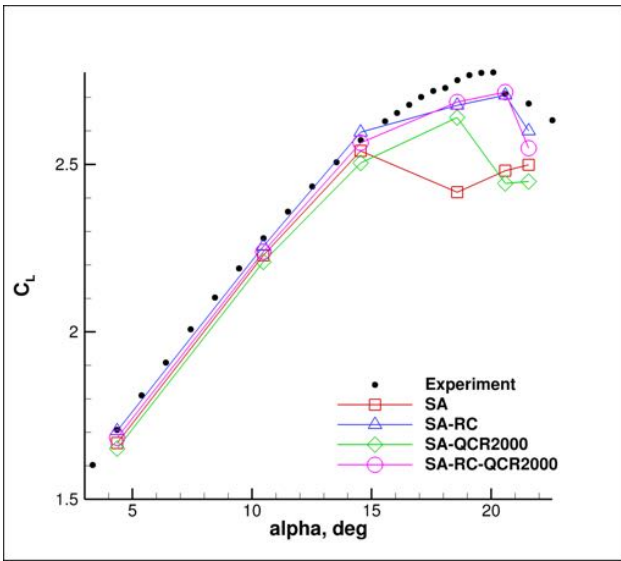


(a) Lift

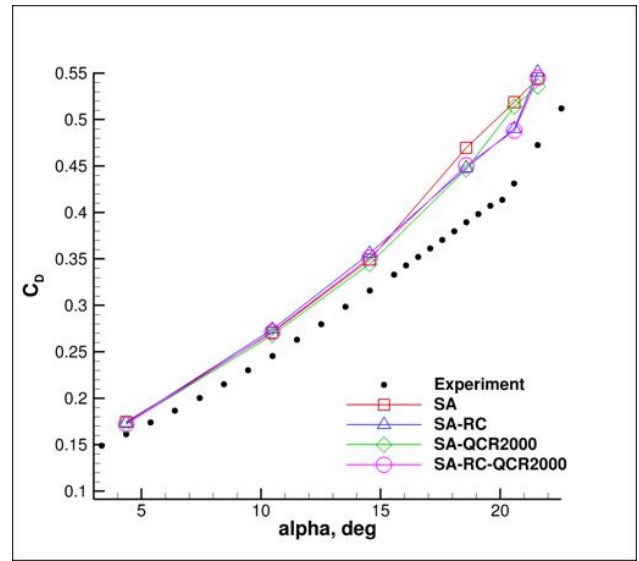


(b) Drag

Figure 20: Lift and drag plots for JSM Case 2c showing the difference between the cold and warm starts.

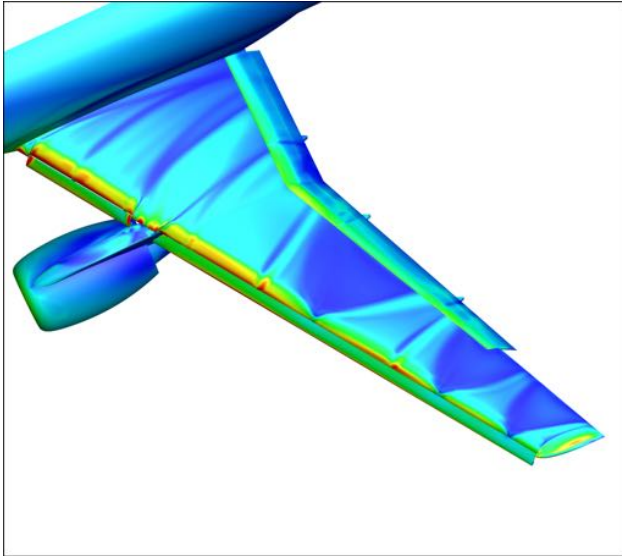


(a) Lift

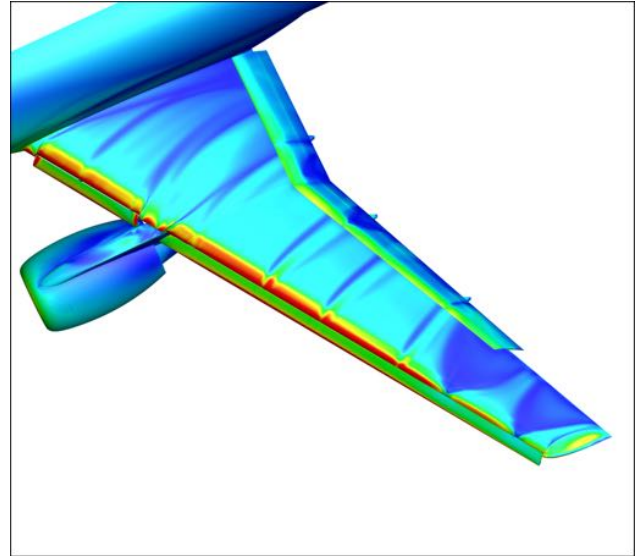


(b) Drag

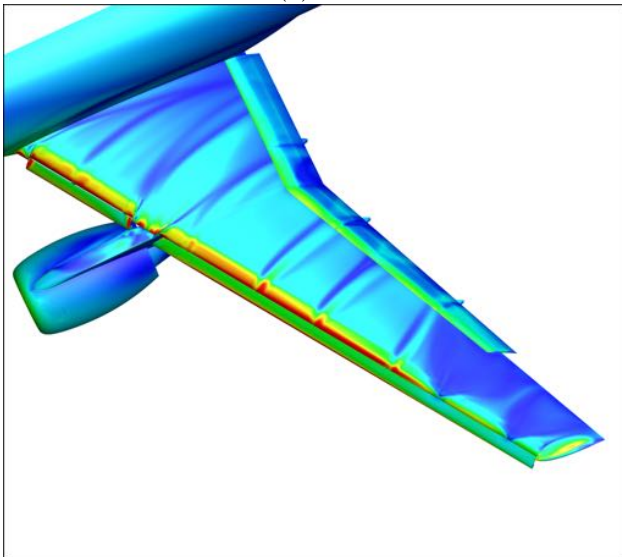
Figure 21: Plots comparing the different turbulence models and their effects on the predicted forces for JSM Case 2c.



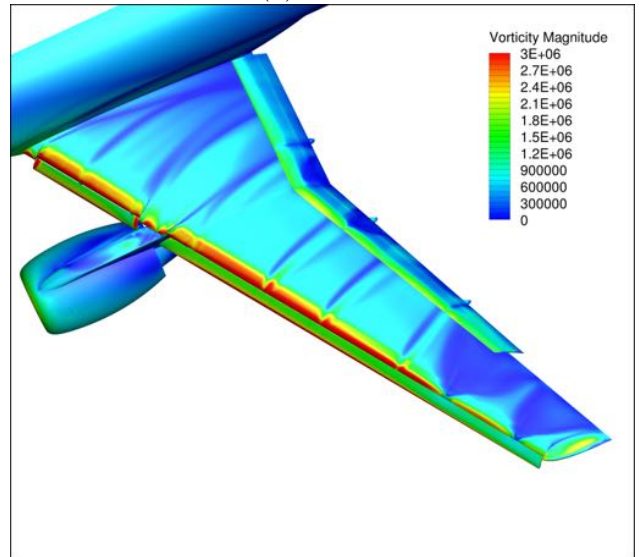
(a) SA



(b) SA-RC

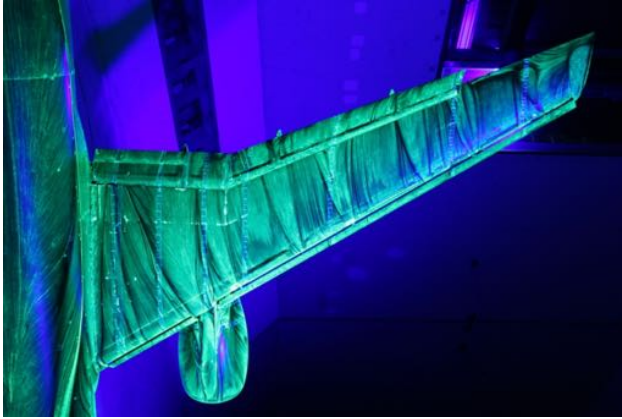


(c) SA-QCR2000

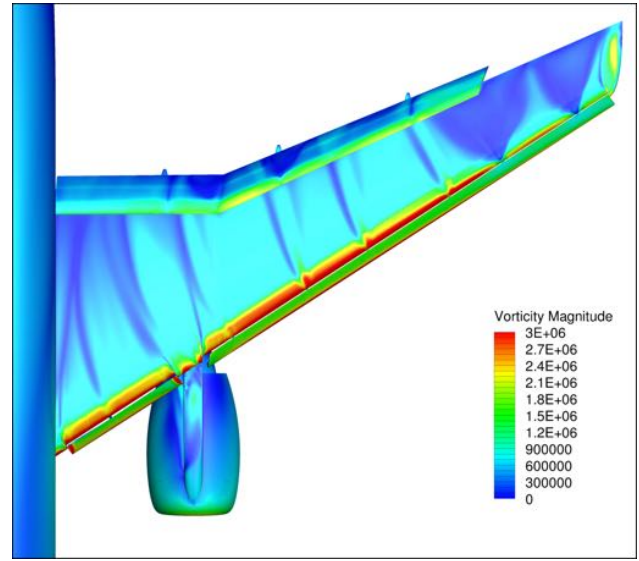


(d) SA-RC-QCR2000

Figure 22: Comparison of the vorticity magnitude over the upper surface of the JSM wing for all four turbulence model variants at 18.58° .

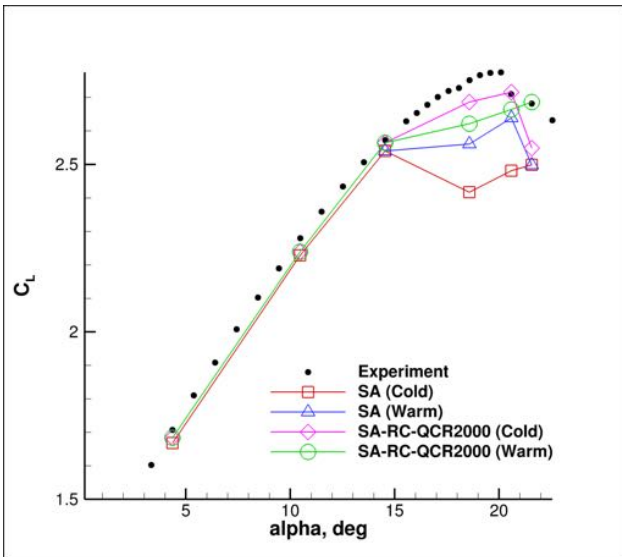


(a) Oilflow

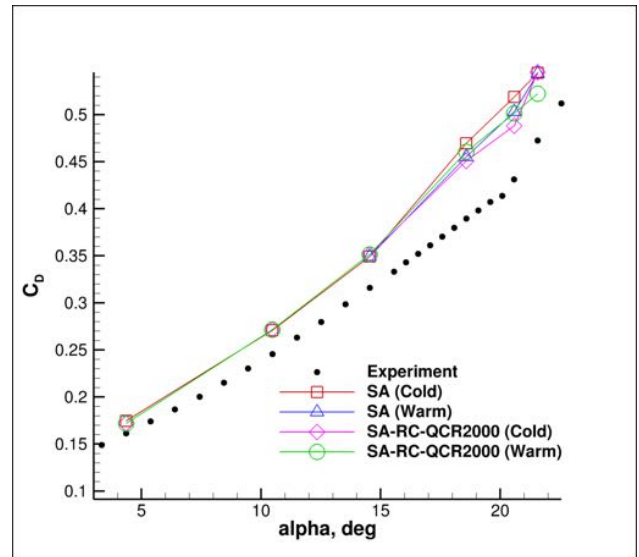


(b) Vorticity Magnitude

Figure 23: Comparison between (a) oilflow images taken from the wind tunnel experiment and (b) vorticity magnitude contour from the CFD.

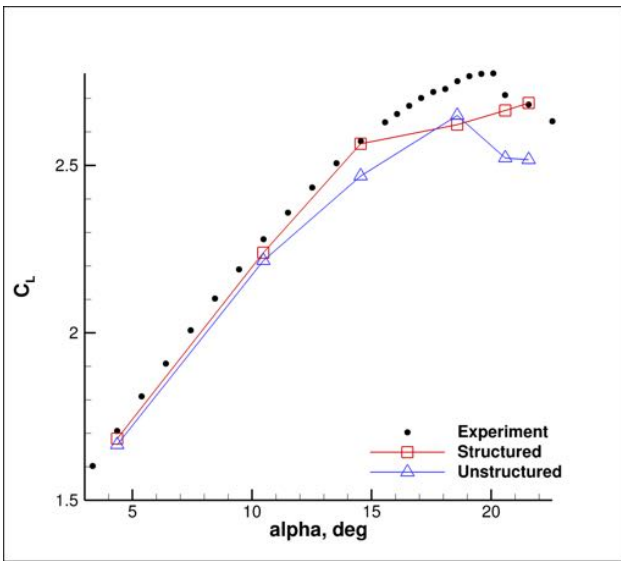


(a) Lift

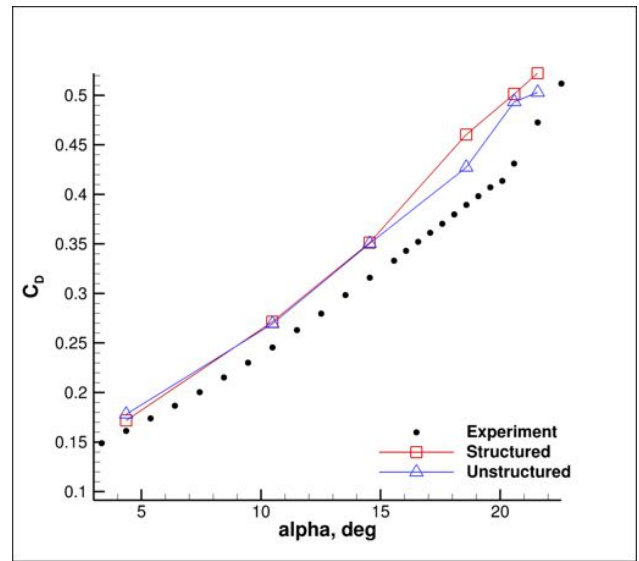


(b) Drag

Figure 24: Comparison between warm and cold starts for different variations of the SA turbulence model.



(a) Lift



(b) Drag

Figure 25: Lift and drag curves for Case 2c as predicted by both the unstructured and structured solvers.